

# Electronic Properties of Nanoclusters in Amorphous Materials



# Electronic Properties of Nanoclusters in Amorphous Materials

By

Mikio Fukuhara

Cambridge  
Scholars  
Publishing



Electronic Properties of Nanoclusters in Amorphous Materials

By Mikio Fukuhara

This book first published 2019

Cambridge Scholars Publishing

Lady Stephenson Library, Newcastle upon Tyne, NE6 2PA, UK

British Library Cataloguing in Publication Data

A catalogue record for this book is available from the British Library

Copyright © 2019 by Mikio Fukuhara

All rights for this book reserved. No part of this book may be reproduced, stored in a retrieval system, or transmitted, in any form or by any means, electronic, mechanical, photocopying, recording or otherwise, without the prior permission of the copyright owner.

ISBN (10): 1-5275-3755-2

ISBN (13): 978-1-5275-3755-2

# CONTENTS

Preface.....	vii
Chapter 1 .....	1
Introduction	
Chapter 2 .....	2
Electronic rules and excess electrons for the formation of amorphous alloys	
2.1 <i>Electronic rules for the formation of amorphous alloys</i>	
2.2 <i>Ab initio molecular orbital calculations of excess electrons</i>	
Chapter 3 .....	8
Local atomic structures of $\text{Ni}_5\text{Nb}_3\text{Zr}_5$ clusters in Ni-Nb-Zr-H amorphous alloys	
3.1 <i>X-ray absorption fine structure (XAFS) analysis</i>	
3.2 <i>Structures of the icosahedral clusters by first-principles molecular dynamics calculation and XAFS measurements</i>	
3.3 <i>Structures and electronic properties of <math>\text{Ni}_5\text{Nb}_3\text{Zr}_5</math> clusters in Ni-Nb-Zr amorphous alloys</i>	
3.4 <i>Local structures and structural phase change in Ni-Zr-Nb amorphous alloys composed of <math>\text{Ni}_5\text{Nb}_3\text{Zr}_5</math> icosahedral clusters</i>	
3.5 <i>Distorted icosahedral <math>\text{Ni}_5\text{Nb}_3\text{Zr}_5</math> clusters in the as-quenched and hydrogenated amorphous <math>(\text{Ni}_{0.6}\text{Nb}_{0.24})_{0.65}\text{Zr}_{0.35}</math> alloys</i>	
3.6 <i>Vacancy analysis in Ni-Nb-Zr-H amorphous alloys by positron annihilation spectroscopy</i>	
3.7 <i>Proton NMR studies of hydrogen diffusion and electron tunneling in Ni-Nb-Zr-H amorphous alloys</i>	
Chapter 4 .....	47
Room temperature Coulomb oscillation and amorphous alloy field effect transistor (AAFET) in Ni-Nb-Zr-H amorphous alloys	
4.1 <i>Coulomb oscillation in a Ni-Nb-Zr-H amorphous alloy with multiple junctions</i>	
4.2 <i>Room temperature Coulomb oscillation in Ni-Nb-Zr-H amorphous alloys with nanofarad capacitance</i>	
4.3 <i>Effect of current on Coulomb oscillation</i>	
4.4 <i>Magnetic field induced Coulomb oscillation in Ni-Nb-Zr-H amorphous alloys</i>	
4.5 <i>Fano Effect on AAFET in Ni-Nb-Zr-H amorphous alloys</i>	
4.6 <i>Room temperature Fabry-Perot (FP) effect on AAFET with particle and wave natures</i>	
Chapter 5 .....	70
Ballistic transport in Ni-Nb-Zr-H amorphous alloys	
5-1 <i>Electronic transport behaviours of Ni-Nb-Zr-H amorphous alloys</i>	
5-2 <i>The effect of degree of amorphousness on electronic transport behaviours</i>	
5-3 <i>Rotating speed effects on electronic transport behaviours</i>	
5-4 <i>Effect of hydrogen content on ballistic transport behaviours</i>	
5-5 <i>Chaotic properties of quantum transport</i>	

Chapter 6 .....	89
Superconductivity, resistivity under pressure, and thermoelectricity	
6-1 Superconductivity of Ni-Nb-Zr-H amorphous alloys under magnetic field	
6-2 Pressure-induced positive electrical resistivity coefficient in Ni-Nb-Zr-H amorphous alloys	
6-3 Electric resistivity and thermoelectricity in Ni-Nb-Zr-H amorphous alloys	
Chapter 7 .....	99
Electric Storage and supercapacitors in amorphous materials	
7-1 AC impedance analysis of a Ni-Nb-Zr-H amorphous alloy with femtofarad capacitance tunnels	
7-2 Electric storage in de-alloyed Si-Al alloy ribbons	
7-3 Super electric storage in de-alloyed and anodic oxidised Ti-Ni-Si amorphous alloy ribbons	
7-4 Supercapacitors in amorphous titania	
7-5 Superior electric storage on amorphous perfluorinated polymer surface	
7-6 Amorphous alumina supercapacitor	
Chapter 8 .....	130
Electronic transport behaviours due to charge density waves	
Chapter 9 .....	136
Conclusion	
References .....	138

## PREFACE

I had a vivid impression that most amorphous alloys glisten notably rather than having a general metallic luster, when I came across metallic amorphous containing metallic glasses at the Institute for Materials Research, Tohoku University, in 2005. I lost no time in elucidating the reason. Since amorphous alloys are generally synthesised from molten alloys using free jet melt spinning at a cooling rate of  $10^1$ – $10^6$  K/s, they are pseudo liquids. From *Ab initio* molecular orbital calculations of excess electrons, we found that many free electrons containing *d* or *f* electrons, in addition to *s* and *p* ones, play a definitive role in the formation of amorphous alloys. Therefore, we established a valence electron rule for amorphous formation based on the analysis results, which stated that the resonance bonding of the amorphous alloys could be caused by *spd* or *sp<sup>f</sup>* hybridisation. The establishment of the rule enabled a person to form new kinds of amorphous alloys.

When I unexpectedly measured the electrical resistivity of amorphous  $\text{Ni}_{42}\text{Nb}_{28}\text{Zr}_{30}$ –H alloys developed as a membrane for hydrogen permeability from 373 to 6 K in He of ambient pressure, I observed an abnormal variation in cooling and heating runs at specific hydrogen concentrations and within a certain temperature range. This was the Coulomb oscillation based on low-temperature electric current-induced voltage oscillation. Further investigations into the effects of Zr and H contents in amorphous  $\{(\text{Ni}_{0.6}\text{Nb}_{0.4})_{100-x}\text{Zr}_x\}_{100-y}\text{H}_y$  ( $x = 30, 35, 40, 45$  and  $50, 5.2 \leq y \leq 22$ ) alloys revealed about five kinds of electrical and electronical transport behaviours, such as room temperature Coulomb oscillation, ballistic transport, electron avalanche, superconducting, semi-conducting, and electric storage. The realisation of room-temperature macroscopic aluminium-oxide amorphous alloy field effect transistor (AAFET) exhibited a one-electron Coulomb oscillation, a Fabry-Periot interface under nonmagnetic conditions, and a Fano effect under a magnetic field. Ballistic transport, which is generally observed in one-dimensional nanometre sized channel at a very low temperature, reached 230 K for amorphous  $(\text{Ni}_{0.39}\text{Nb}_{0.25}\text{Zr}_{0.35})_{78.8}\text{H}_{21.2}$  alloys.

However, we found a superior electric storage effect on a nanometre-sized uneven surface with an insulating resistance for amorphous titanium and aluminum oxides, and perfluorinated polymer, resulting from both the quantum-size effect and an offset effect from positive charges at oxygen-vacancy sites and C=O and N-H radicals with permanent dipoles, respectively. A common requirement for electric storage is an amorphous structure.

To elucidate on the various electronic properties, we analysed cluster-vacancy structures composing amorphous alloys, using XAFS, XANES, and positron annihilation spectroscopy and proton NMR analyses. In our results, we found that the distorted icosahedral  $\text{Ni}_5\text{Nb}_3\text{Zr}_5$  clusters with tetrahedral H sites and tetrahedral vacancy sites play important roles in various electron transport phenomena. The cluster was recognised as a “perovskite-like cluster” in amorphous compounds. These behaviours could be explained by the macroscopic CDW properties of amorphous alloys. These new findings are expected to give rise to a new era of amorphous materials.





# CHAPTER 1

## INTRODUCTION

The amorphous alloys, which are the last frontier of metals and metallic alloys, are peculiar metallic alloys in that they lack, on the nanoscale, the long-range translational order of crystalline alloys, as they have grain boundaries and lattice imperfections [1, 2]. Since 1960, when Klement *et al.* [3] discovered amorphous alloys in the Au-Si system, work has been carried out on the preparation and properties of various amorphous alloys [4–7]. Amorphous alloys have characteristic physical and chemical properties, such as high strength, high corrosion resistance, and superior electronic properties, which are significantly different from the corresponding crystalline alloys. Much attention has been devoted to the amorphous forming ability of elements of different types in amorphous alloys [6]: *i.e.*, their cluster structures [8] and potential applications. Special interest focuses on glass-forming ability associated with formation of metastable polyhedra [8], and glass transition by a free volume related kinetic phenomenon [9]. However, in addition to these characteristics, it is also important to examine their cluster characteristics in order to understand electronic properties of amorphous materials. We have reported electronic properties such as Coulomb oscillation, ballistic transport, superconductivity, and electric storage in terms of atomic morphology of subnanometre-sized clusters composing the amorphous alloys and titanium and aluminium-oxides, and perfluorinated polymer. These phenomena are reasonably similar to those appearing in many different types of crystalline charge-density-wave (CDW) conductors with energy gaps at the Fermi surface. We report that low-dimensional CDW phenomena are characterised by five types of nonlinear, anisotropic behaviours involving their electronic characteristics. In contrast to crystalline perovskite compounds with various electronic properties, we especially focused on analysis of sub-nanometre-sized  $\text{Ni}_5\text{Nb}_5\text{Zr}_5$  icosahedral cluster in Ni-Nb-Zr-H amorphous alloys. In our results, we found that the cluster has perovskite-like properties in amorphous compounds. These findings provide new insights into electron transport devices in this century, which are based on cluster science and technology. However, to the best of our knowledge, no work has been carried out previously on electronic studies of amorphous materials, especially amorphous alloys with various properties.

## CHAPTER 2

### ELECTRONIC RULE AND EXCESS ELECTRONS FOR FORMATION OF AMORPHOUS ALLOYS

#### *2.1 Electronic rule for formation of amorphous alloys [10, 11]*

Pauling has derived the concept of “valence electron” for elements when they are bonded in the crystalline metallic state [12]. Pauling defined that the valence number of metals cannot be greater than six in the valence-bond theory of metals. Figure 1 is a representative example, which presents values of metallic valence for the transition elements of the first long period [13]. However, the valence electron theory for intermetallic compounds has not been as fully developed during the past century as for other compounds, such as organic and inorganic ones, because of

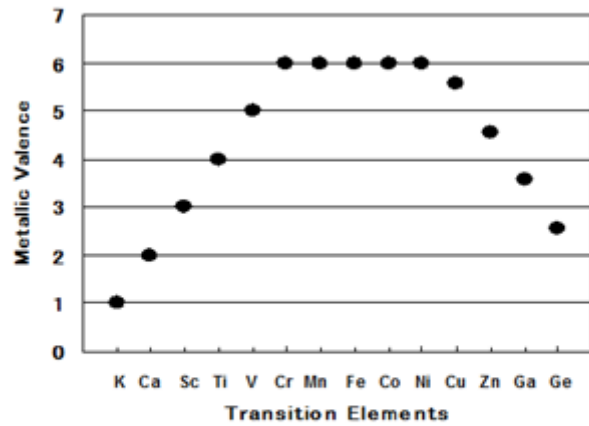


Fig. 1 Values of metallic valence for the elements of the first long period.

their undefined composition [14]. Only the Hume-Rothery interpretation of the valence electron concentration rule for intermetallic compounds has been vigorously investigated [15]. The valence electrons are defined as outer freely moving  $s$  and  $p$  or  $d$  electrons that are not bound to any particular cations. The decrease in both the potential and the kinetic energies of the valence electrons due to the unsynchronised resonance of electron-pair bonds is responsible for crystalline metallic bonding. Therefore, the resonance energy of the metallic orbital is very sensitive to the form of the cyclic potential energy that is associated with the crystal system.

On the other hand, the distinguishing feature of amorphous alloys without a crystal structure is the randomness of their potential energy [6]. The potential energy minimum among atoms in the multi-component amorphous alloys is not as rigid as that of crystal alloys, so that the wave functions of these electrons are irregularly spread out much more than those of the crystalline metallic valence electrons. Therefore, we cannot expect the unsynchronised resonance effect by the cyclic potential energy to form the amorphous phases. Furthermore, the amorphous alloys have two bonding types, metal/metal and metal/metalloid [16], and the atomic configurations of the amorphous alloys differ between them. The amorphous structure of the former is composed of icosahedral clusters, while the structural feature of the alloy of the latter is the construction of a network of atomic configurations consisting of trigonal prisms [17] and transformed tetragonal

dodecahedrons [8].

Our interest lies in studying thermal stability of amorphous alloys as the function of their valence electron concentration (*VEC*) in terms of amorphous metallic bonding, using 121 types of amorphous alloys. We consider that the electron contribution provides useful information when interpreting the bonding mechanism of the amorphous alloys. Indeed, the electronic structure of Pd- and Zr-based bulk amorphous alloys has been examined by X-ray photoelectron spectroscopy (XPS) [18]. Additionally, the relationship between stability and electronic structure for Zr-based ternary amorphous alloys has been investigated by band calculation using LMTO-ASA method [19]. However, as far as we know, no research has been previously carried out on the statistic valence electron contribution to bonding nature responsible for the thermal stability of a large number of amorphous alloys. Inoue *et al.* proposed the three empirical rules for an amorphous alloy-forming ability [20]. However, the use of crystal element radii puts constraints on these rules. Indeed, there are some examples that violate these rules.




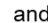
In general, the thermal stability of metallic alloys can be evaluated by adjusting the height of the Fermi level to the *VEC* proposed by Bilz [21]. The *VEC* in the amorphous alloys ( $II_A, III_B, IV_C, V_D, VI_E, VII_F, VIII_G$ ) and ( $II_A, III_B, IV_C, V_D, VI_E, VII_F, VIII_G$ ) ( $M_x$ )<sub>w</sub> ( $M = B, C, Si, P, Ge, Sn, Sb, Bi$ ), respectively, of group II to VIII elements has been defined as follows [22, 23]:

$$VEC = II_A + III_B + IV_C + V_D + VI_E + VII_F + VIII_G \text{ for metal/metal type,} \quad (1)$$

$$VEC = II_A + III_B + IV_C + V_D + VI_E + VII_F + VIII_G + \sum M_i X W \text{ for metal/metalloid type,} \quad (2)$$

where  $A, B, C, D, E, F$ , and  $G$  are atomic fractions,  $A+B+C+D+E+F+G=1$  and  $\sum M_i X=1$ . The *VEC* for 2 kinds of binary, 89 kinds of ternary, 16 kinds of quaternary, and quintuple of 6 kinds Pd-, Zr-, Fe-, Ni-, Co-, Cu-, Mg-, Ti-, Hf-, Au-, Al-, Pt-, La-, Ca-, and Be- based amorphous alloys have been calculated using electron valences from 42 of their constituent elements. As an intrinsic parameter for thermal stability of the amorphous alloys, we selected a glass transition temperature of  $T_g$ . The data (see Table 1) used in this study has been taken from literature [24] on 121 amorphous alloys with  $T_g$  compositions. After we assigned the electron valence from 1 to 15 for  $s$ ,  $p$ ,  $d$ , and  $f$  orbits in all elements, taking multiple orbital electron hybridisation into consideration and based on the standard method of the least squares, we repeatedly calculated until we obtained the best linearity for the correlation between  $T_g$  and *VEC*. The best result is shown in Fig. 2, for metal/metal and metal/metalloid bonding types. Both type alloy groups show fairly good linearity:  $r=0.887$  and  $0.866$ , respectively. The metallic valence for all elements used in this section is shown in Table 2 using a periodic table format with four kinds of  $s$ -,  $p$ -,  $d$ -, and  $f$ - electron blocks. Cooper [25] has classified all elements in the periodic table into four kinds of  $s$ -,  $p$ -,  $d$ -, and  $f$ - electron blocks: the  $s$ - block includes the Ia and IIa group elements; the  $p$ - includes the IIIb, IVb, Vb, VIb, VIIb and 0 group elements, the  $d$ - includes the IIIa, IVa, Va, VIa, VIIa, VIIIa, Ib and IIb group elements; and the  $f$ - includes the lanthanide and actinide group elements. We used his proposal for the classification of the elements in Table 1. Although Al and Pb belong to the  $p$ -electron block, they were treated as 100 % metallic/metallic and 50% metallic/50% metalloid

elements, respectively. The valence values for other elements, Ca, Sc, Zn, Ga, In, Er, and Tl were 2.4, 3.0, 2.0, 3.0, 3.0, 3.0, and 3.0, respectively.

Table 1 Electron valence for electrons used in this study.  ,  ,  and  are *s* -, *p* -, *d* - and *f* - electron blocks.

Period icity	2 (IIa)	3 (IIIa)	4 (IVa)	5 (Va)	6 (VIa)	7 (VIIa)	8 (VIII)	9 (VIII)	10 (VIII)	11 (Ib)	12 (IIb)	13 (IIIb)	14 (IVb)	15 (Vb)
2	Be 2.4											B 3.0	C 4.0	
3	Mg 2.4											Al 3.0	Si 4.0	P 5.0
4	Ca 2.4	Sc 3.0	Ti 4.0	V 5.0	Cr 6.0	Mn 6.0	Fe 6.1	Co 6.1	Ni 6.2	Cu 5.8	Zn 2.0	Ga 3.0	Ge 4.0	
5		Y 3.0	Zr 4.5	Nb 5.4	Mo 6.1			Rh 6.2	Pd 6.5	Ag 6.0		In 3.0	Sn 4.0	Sb 5.0
6		La,Ce, Nd,Er, Tm 3.0	Hf 4.6	Ta 5.5	W 6.3				Pt 6.6	Au 7.2		Tl 3.0	Pb 4.0	Bi 5.0

As can be seen from Fig. 2,  $T_g$  (K) can be expressed as

$$T_g = 131VEC + 65 \quad (r=0.887) \text{ for metal/metal bonding type} \quad (3)$$

$$T_g = -240VEC + 2408 \quad (r=0.866) \text{ for meta/metalloid bonding type.} \quad (4)$$

For metal/metal type amorphous alloys, a positive slope means that their thermal stability increases when the valence also increases. In crystalline metals, an increase in the valence electron correlates to a reduction of atomic distance due to the unsynchronised resonance of electron-pair bonds, leading to higher strength and melting points [12]. Therefore, metal/metal type amorphous alloys also follow the valence electron rule, which is predicted using crystalline metallic valence bond theory. However, for metal/metalloid type-metallic amorphous alloys, an increase in  $VEC$ —*i.e.*, an increase in the amount of metalloid elements—indicates deterioration in the thermal stability of the amorphous.

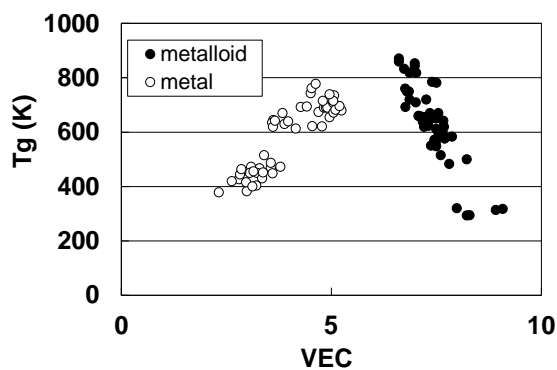


Fig. 2 The relationship between  $T_g$  and  $VEC$  for 112 types of amorphous alloys: open and solid circles present metal/metal and metal/metalloid bonding types, respectively.

Thus, the stable region for formation of the amorphous phase would be  $2.3 < VEC < 5.2$  and  $6.6 < VEC < 9.1$  for metallic and metalloid-type metallic amorphous, respectively. The most optimum condition for the formation of amorphous alloys with the highest  $T_g$  would be  $VEC \doteq 6$ . This means that transition metal elements with higher valence (e.g., group VIII and Ib elements) are the most desirable ones for the formation of amorphous alloys with higher  $T_g$ . In addition, it is empirically confirmed that the inorganic compound of transition metals is stable when  $VEC \leq 8.8$  [22].

To certificate the application of  $VEC$  for the electronic rule associated with thermodynamic stability of amorphous alloys (*i.e.*, the reliability of metallic valences in Table 1), we here calculated the stability for anionic clusters by an excess amount of electrons transferring from inner orbital  $d$  or  $f$  electrons, in comparison with the stability for neutral ones [26]. Since it is very difficult to precisely calculate the stability of polyhedral clusters constituting of amorphous alloys at the present time, we chose magnesium based amorphous alloys as a representative amorphous alloy. In Mg-Ni-Nd, Mg-Cu-Sn, and Mg-Cu-Y systems from Table 2, it is anticipated that anionic magnesium clusters [27] will be formed by an electron transfer from the Ni, Nd, Sn, and Y elements (Fig. 2) using the *Ab initio* molecular orbital calculations described in 1.2.

Table 2. Values of  $T_g$  and  $VEC$  for 121 kinds of amorphous alloys used in this section.

metal/metal type	VEC	$T_g(K)$	Hf65Cu25Al10	4.53	762	Pd73.5Cu10Si16.5	7.21	652
Zr40Nb20Al10Ni10Cu20	4.96	728	Hf65Ni25Al10	4.63	778	Pd69Cu14.5Si16.5	7.16	657
Zr41Be23Ti14Cu12Ni10	4.27	693	Y56Al24Co20	3.62	636	Pd77.5Cu6Si16.5	7.24	635
Zr41.2Ti13.8Ni10Cu12.5Be22.5	4.15	613	La55Al25Ni20	3.56	487	Pd73.8Cu5.7Si20.5	7.48	660
Zr50Nb10Al10Ni10Cu20	4.87	691	La55Al25Cu20	3.60	449	Pd84Si14Ge2	7.26	634
Zr50Cu40Al10	4.87	703	Be20Nb15Zr65	3.98	640	Pd83Si10Ge7	7.32	624
Zr55Cu30Al10Ni5	4.83	690	Be25Nb15Zr60	3.89	630	Pd48Ni32P20	7.71	582
Zr60Ni20Cu20	4.96	655	Be30Nb20Zr50	3.84	670	Pd37.5Ni37.5P25	7.67	619
Zr65Al7.5Ni10Cu17.5	4.55	622	Be35Nb10Zr55	3.66	642	Pt42.5Cu27Ni9.5P21	7.61	515
Zr65Ni10Cu5Al7.5Pd12.5	4.70	674	Be35Nb5Zr60	3.62	620	Pt60Ni15P25	8.23	500
Ti41.5Cu47.5Hf5Zr2.5Ni7.5Sn1	5.24	680	Be35Nb2.5Zr62.5	3.59	635	Pt64Ni16P20	7.81	483
Ti45Cu40Ni7.5Zr5Sn7.5	4.91	690	Ca65Mg15Zn20	2.32	379	Ni40Fe40P20	7.50	650
Ti50Ni25Cu25	5.05	707	Ca57Mg19Cu24	3.22	404	Ni40Fe30Pd10P20	7.55	600
Ti50Cu25Ni25	5.05	707	Ca60Mg20Ag20	3.12	401	Ni40Fe20Pd20P20	7.60	600
Ti60Cu30Ni10	4.78	621	Y36Sc20Al24Co20	3.62	645	Ni45Pd35P20	7.58	588
Ti61Cu23Ni16	4.80	715	metalloid/metal type	VEC	$T_g(K)$	Ni75Si8B17	7.51	782
Mg65Cu15Ag5Pd5Gd10	3.29	430	Pd40Ni40P20	7.70	576	Fe48Cr15Mo14Er2C15B6	6.99	843
Mg65Ni20Nd15	3.29	467	Pd30Ni50P20	7.69	583	Fe80P20	7.35	650
Mg70Ni15Nd15	3.09	473	Pd50Ni28P22	7.87	584	Fe82B18	6.76	760
Mg75Ni15Nd10	3.06	450	Pd40Cu40P20	7.50	548	Fe70Nb10B20	6.74	833
Mg75Ni20Nd5	3.23	450	Pd50Cu30P20	7.49	562	Fe70Zr10B20	6.61	860
Mg77Ni18Nd5	3.15	456	Pd60Cu20P20	7.58	596	Fe70W10B20	6.86	819
Mg80Cu15Sn5	2.99	383	Pd20Cu40Ni20P20	7.38	551	Fe70Hf10B20	6.61	871
Mg80Ni10Nd10	2.86	453	Pd25Cu30Ni25P20	7.46	572	Fe40Ni40P14B6	7.35	670
Mg80Cu10Y10	2.80	427	Pd30Cu30Ni20P20	7.46	569	Fe41.5Ni41.5B17	6.87	720
Mg85Cu5Y10	2.63	420	Pd40Cu30Ni10P20	7.48	571	Fe79Si10B11	7.02	818
Mg75Cu15Y10	2.97	416	Pd50Cu20Ni10P20	7.56	597	Fe80P13C7	7.26	720
Mg75Cu10Y15	2.83	445	Pd60Cu10Ni10P20	7.65	604	Fe77Mn4B19	6.80	750
Mg70Cu10Y20	2.86	464	Pd40Ni25Fe15P20	7.64	603	Fe80P17Al3	7.01	710
Cu42Zr42Al8Ag8	7.15	715	Pd40Ni20Fe20P20	7.63	598	Fe83P15B2	7.08	660
Cu46Zr45Al7Y5	5.05	672	Pd15Ni65P20	7.67	642	Fe80Pd2B18	6.77	693
Cu45Zr45Ag10	5.10	682	Pd27Ni53P20	7.68	620	Fe80B17Si3	6.85	750
Cu45Zr20Hf25Ag10	5.20	696	Pd74Cu10Si16	7.18	639	Fe40Ni40P20	7.50	612
Cu55Zr30Ti10Pd5	5.07	735	Pd77Cu6Si17	7.27	636	Fe83P14Si3	7.09	660
Al25La55Cu20	3.56	470	Pd78Cu6Si16	7.21	620	Au53.2Pb27.5Sb19.2	8.92	314
Al25La55Ni20	3.79	473	Pd79Ag4.5Si16.5	7.27	640	Au50Pb22.5Sb22.5	9.08	318
Al20Zr55Ni25	4.51	743	Pd77Cu5Si18	7.26	655	Au63.5Pb11.5Ge14Si9	7.99	320
Al15Zr60Cu25	4.42	694	Pd75Cu8.5Si16.5	7.22	645	Au78Ge14Si8	8.23	294
Al87Ni10Zr3	3.38	452	Pd79Au4Si17	7.35	646	Au77Ge14Si9	8.30	295
Al85Ni10Zr5	3.40	515	Pd73Au7Si20	7.55	670	Co75Si15B10	7.40	785
Hf60Ni20Cu20	4.96	739	Pd80Cu3.5Si16.5	7.26	640	Co48Cr15Mo14C15B6Tm2	6.99	853

In Table 2, our definitive valence for Mg is 2.4. This value means the magnesium atom is partially charged. We then calculated the monoanion  $Mg_3^-$  (average valence is 2.33) and  $Mg_4^-$  clusters (average valence is 2.25) taking the electron transfer from other constituent elements into consideration. The initial structure for optimisation is a part of crystalline magnesium.  $Mg_3^-$  has a

three-membered ring structure ( $D_{3h}$ ), while, for  $Mg_4^-$ , two types of structure are possible: a four-membered ring and a tetrahedron. Full optimisation of  $Mg_4^-$  gives tetrahedron ( $C_{3v}$ ) an equilibrium structure. Comparing the optimised structures between the neutral cluster and the monoanion, the magnesium bond lengths of the monoanion are shortened: 0.3475 (0.3475) nm at the CBS-QB3 (G3B3) level for neutral  $Mg_3$  and 0.3140 (0.3145) nm for the monoanion  $Mg_3^-$ ; 0.3165 (0.3178) nm for neutral  $Mg_4$  and 0.3127 (0.3140) nm for the monoanion  $Mg_4^-$ . The energy difference between the neutral cluster and the monoanion indicates that the monoanion is more stable than the neutral clusters by 264 (283) meV/atom for  $Mg_3$  and 286 (233) meV/atom for  $Mg_4$  at the CBS-QB3 (G3B3) level, respectively. We can, therefore, conclude that the increase in the valence of magnesium stabilises the cluster structures and positively affirms the application of *VEC* for the electronic rule associated with the stability of amorphous alloys.

In Table 1, the valences are somewhat larger than those based on crystalline metallic valence bond theory [13]. This suggests that many free electrons containing  $d$  or  $f$  electrons, in addition to  $s$  and  $p$  ones, play a definitive role in the formation of amorphous alloys. Therefore, the resonance bonding of the amorphous alloys could be caused by  $spd$  or  $spf$  hybridisation. As corroborating evidence, X-ray photoelectron spectroscopy analysis [28] of amorphous alloy  $Zr_{55}Al_{10}Cu_{30}Ni_5$  suggested that stabilisation in the amorphous phase is derived from the formation of a pseudo gap below the Fermi energy  $E_F$  due to  $spd$  hybridisation. When periodicity in transition metal elements increases, it is expected that the width of  $d$ -band will also increase and consequently promote  $spd$  hybridisation. Furthermore, since the amorphous alloys are pseudo-liquid, the liquid would be formed by multiple orbital electron hybridisation. Lastly, we applied the new rule to metallic type- $Cu_{45}Zr_{(45-x)}Hf_xAg_{10}$  alloys on trial. According to the rule, *VEC* of  $Cu_{45}Zr_{20}Hf_{25}Ag_{10}$  amorphous alloy is 5.26, which is closed to the stable limit, 5.3. Since *VEC* in Hf is slightly larger than Zr due to the difference in the width of  $d$ -band, we can estimate that it is difficult to form stable amorphous alloys with Hf content over 25%. Indeed, the experimental result coincided perfectly with the estimation [29].

This study makes the electronic contribution for thermal stability of most of all the amorphous alloys clear. The primary study in this paper will lead to an amorphous alloy bonding theory that Pauling has not considered. It also provides some guidelines for the selection of amorphous forming compositions that prevent the formation of crystalline phases and alloy design of promising amorphous alloys with functional properties, such as electronics, optics, and catalysis.

## 2.2 *Ab initio* molecular orbital calculations of excess electrons [30]

Since the formation mechanism of amorphous alloys has not been clearly elucidated, we will investigate the effect of excess electrons accommodated in hcp Mg and various Mg clusters as a representative example, using density functional theory-based calculations in order to reveal the role of conduction electron concentration in the amorphous-forming ability and thermal stabilities of Mg-based amorphous alloy. The role of conduction electron concentration is one of the key roles to reveal the mechanism.

The search for the equilibrium structures of the clusters was performed using density functional theory (DFT) with the Becke3-Lee-Yang-Parr (B3LYP) functional and the 6-311+G (d) basis set as implemented in the GAUSSIAN-03 package [31]. The important feature of the density functional method is characterised by many electron correlations via the phenomenological exchange-correlation potential.

From the point of the electronic structure, the density of states (DOS) revealed the effect of excess electrons. The DOS of the neutral hcp Mg exhibits a “free-electron-gas” parabolic behaviour until  $-1.5$  eV below the Fermi level, due to weak  $s$ - $p$  hybridisation and the strong contribution of the  $p$  bands to the total DOS [32, 33]. However, the DOS

of the expanded lattice showed a high concentration of bands with small dispersions and the appearance of a spiky structure, which is reported for quasicrystalline materials [34]. The spiky peaks are a state signature, which is preferentially localised around the structural cluster [34, 35]. Since our aim is to understand the formation mechanism of Mg-based amorphous alloys, we then investigated the effects of excess electrons on hexagonal close-packed (hcp) Mg and the model clusters, which can be explained by an inflation process. For the clusters ( $\text{Mg}_7$ ,  $\text{Mg}_{10}$ , and  $\text{Mg}_{17}$ ) and hcp Mg, the  $c/a$  ratio increases proportionally with the concentration of excess electrons and the cell volume also expands. This suggests that the increase in the conduction electron concentration of Mg in amorphous alloys possibly stabilises the cluster structures. The higher  $c/a$  ratio accompanied by distortion suggests that the melting point would be lowered in the charge state. The pseudogap by  $s$ - $p$  mixing at the Fermi level is weakened in the expanded cell with a distorted  $c/a$  ratio and the spiky structure is mainly created by  $p$ -bands. This means it has preferential localisation around the structural cluster. In other words, the expanded volume and the distorted  $c/a$  ratio by the charge transfer from additives suppress the crystallisation of super-cooled liquid. Figure 3 summarises that the formation of multiply charge anion  $\text{Mg}_n$  is stabilised by electron transfer from Ni, Nd, Cu, Sn, and Y elements with many free electrons.

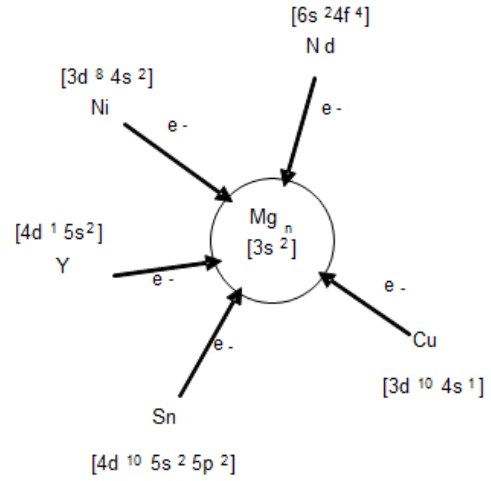


Fig. 3 Formation of the multiple charge anion  $\text{Mg}_n$  formed by an electron transfer from Ni, Nd, Cu, Sn, and Y elements.

## CHAPTER 3

### LOCAL ATOMIC STRUCTURES OF $\text{Ni}_5\text{Nb}_3\text{Zr}_5$ CLUSTERS IN NI-NB-ZR-H AMORPHOUS ALLOYS

We recently found that melt-spun flexible amorphous  $[(\text{Ni}_{0.6}\text{Nb}_{0.4})_{1-x}\text{Zr}_x]_{100-y}\text{H}_y$  ( $0.30 \leq x \leq 0.50$ ,  $0 \leq y \leq 20$ ) alloys show semi-conductivity, superior conductivity (ballistic) and super-conductivity; current-controlled electron avalanches; and Coulomb oscillation as a function of hydrogen content [36]. In particular, the amorphous alloy  $(\text{Ni}_{0.36}\text{Nb}_{0.24}\text{Zr}_{0.40})_{90}\text{H}_{10}$  exhibited Coulomb dot oscillation at room temperature [37] and magnetic-field-induced Coulomb oscillation at 200 K [38]. Furthermore, a Nyquist diagram of a semitrue circle of the alloy with a total capacitance of 17.8  $\mu\text{F}$  [39] showed that the material could be regarded as a dc/ac converter. From these electronic behaviours, we infer that Zr-Ni-Nb clusters, coupled with H, play a decisive role in the promising electronic properties observed in these amorphous alloys, as well as in the familiar Perovskite crystal phase.

#### 3.1 X-ray absorption fine structure (XAFS) analysis [40]

To elucidate the hydrogen effect on the metallic bonding configuration, we measured the X-ray Absorption Fine Structure (XAFS) spectra of the Ni-Nb-Zr amorphous alloy films with two different chemical compositions—*i.e.*  $\text{Ni}_{42}\text{Nb}_{28}\text{Zr}_{30}$  (hereafter referred to as Zr30-H0)—and  $\text{Ni}_{36}\text{Nb}_{24}\text{Zr}_{40}$  (Zr40-H0), and their hydrogen-charged compositions—*i.e.*  $(\text{Ni}_{42}\text{Nb}_{28}\text{Zr}_{30})_{0.91}\text{H}_{0.09}$  (Zr30-H9) and  $(\text{Ni}_{36}\text{Nb}_{24}\text{Zr}_{40})_{0.89}\text{H}_{0.11}$  (Zr40-H11). Although both Zr30-H0 and Zr40-H0 are amorphous [42], the hydrogen permeation characteristic of the latter is higher than that of the former [43]. XAFS as one category of X-ray absorption spectroscopy is a powerful tool for the structural analysis of amorphous materials because the useful information of the local structure around an element of interest can be obtained by tuning the photon energy to the absorption edge of the specific element [44]. By analysing the XAFS oscillation in the X-ray absorption spectra of the Ni-Nb-Zr (-H) alloys measured at the Ni, Nb, and Zr K-edges, we obtained the local structure around these three elements. The results revealed that there are significant differences in the behaviour of the structural change between the Zr-30at% and Zr-40at% samples when hydrogen is charged.

The XAFS spectra were measured at the bending-magnet beamline BL14B2 [45] of the Large-Scale Synchrotron Radiation Facility (SPring-8) in Hyogo, Japan. The incident X-rays were monochromatised by a silicon double crystal monochromator. The net planes used were (311) for the Nb and Zr K-absorption edges, and (111) for the Ni K-absorption edge. The higher harmonics of the incident X-rays were reduced by two Rh-coated mirrors. The spectra were taken in a normal transmittance mode. To obtain the appropriate X-ray absorption intensity, the two sheets of ribbon



had to be stacked in the Nb K- and Zr K-edge measurements, while one sheet of ribbon was the optimum thickness for the Ni K-edge. The samples were cooled down to ~20 K in order to avoid thermal disturbance. The extraction of the XAFS oscillation from the spectra, normalisation by edge-jump, and Fourier transformation were performed by the Athena code [46]. The curve-fitting analysis was carried out in *R*-space by a code Artemis. The XAFS oscillation function  $\chi(k)$  is written as

$$\chi(k) = \frac{S_0^2 N_i F_i(k)}{k r_i^2} \exp\left(-2k^2 \sigma_i^2 - \frac{2r_i}{\lambda_i(k)}\right) \sin(2kr_i + \phi_i(k)) \quad (5)$$

where the electron wave vector  $k$  is defined as

$$k = [2m(E - E_0)/\hbar^2]^{1/2} \quad (6)$$

and  $S_0^2$  is the amplitude reduction factor;  $N_i$  the number of atoms in the  $i$ th shell;  $F_i(k)$  the backscattering amplitude of the  $i$ th neighbour atom;  $r_i$  the mean distance between the absorbing atom and the  $i$ th shell;  $\sigma_i^2$  the mean squared relative disorder (MSRD) between the absorbing atom and an atom in the  $i$ th shell;  $\phi_i(k)$  the phase shift; and  $\lambda_i(k)$  the mean-free path of the photoelectron. In the code Artemis,  $F_i(k)$ ,  $\phi_i(k)$ , and  $\lambda_i(k)$  were theoretically calculated by the code, FEFF6L. The other parameters,  $N_i$ ,  $r_i$ ,  $\sigma_i^2$ , and  $E_0$ , are treated as fitting the parameters in the curve-fitting analysis. In this analysis,  $S_0^2$  is assumed to be unity.

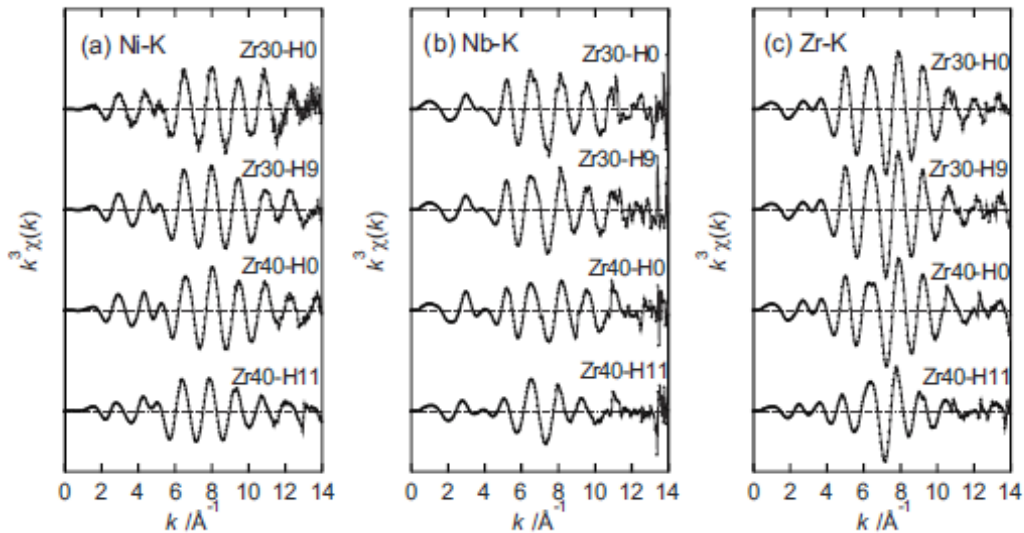


Fig. 4 XAFS oscillations extracted from the X-ray absorption spectra of Zr30-H0, Zr30-H9, Zr40-H0, and Zr40-H11 amorphous alloys measured at the (a) Ni, (b) Nb, and (c) Zr K-edges. Note that the oscillations shown here are weighted by  $k^3$ .

Figures 4(a), (b), and (c) show the  $k^3$ -weighted XAFS oscillations extracted from the absorption spectra of the Zr30-H0, Zr30-H9, Zr40-H0, and Zr40-H11 amorphous alloys measured at the Ni, Nb, and Zr K-edges, respectively. All the oscillation patterns show simple curves, as typically seen

for amorphous materials. The Zr K-edge XAFS oscillations of Zr30-H0 resemble that of the Ni-Nb-Zr alloys with the same chemical composition reported by Sakurai *et al* [47]. The XAFS oscillations for all the K-edges in Zr30-H0 are almost identical with those of Zr30-H9. However, the oscillations of Zr40-H11 are significantly different from those of Zr40-H0, indicating distinct structural change caused by hydrogenation.

The absolute values of Fourier transforms (FTs) of the  $k^3$ -weighted XAFS oscillations ( $|F(r)|$ ) are depicted in Figs. 5(a), (b), and (c) for the Ni-, Nb-, and Zr K-edge oscillations, respectively. The analysed FT ranges are  $2.7 - 13.3 \text{ \AA}^{-1}$ ,  $3.0 - 12.0 \text{ \AA}^{-1}$ , and  $2.9 - 13.5 \text{ \AA}^{-1}$  for the Ni, Nb, and Zr K-edges, respectively. Each FT spectrum gives basically similar information to the partial radial-distribution-function (RDF) around the core-excited atoms. Note, however, that the apparent inter-atomic distances in the spectra shift on the shorter side by several tenth of Ångström from the average values of the atomic distances obtainable in a diffraction method, since the phase shift correction has not been carried out. At  $r > 4 \text{ \AA}$ , there is no clear structure in the FT spectra for all the samples at the three absorption edges, indicating that there is mostly no longer-range ordering in the amorphous alloys. The electron scattering from the atoms locating at longer position than  $4 \text{ \AA}$  in these amorphous alloys only piles up a little in the background of the FT spectra. The closest neighbour peaks of the FT spectra from the Ni K-edge for all the samples are asymmetrical (Fig. 5[a]), suggesting that each of these peaks consists of two or more components. Firstly, there should be two components which come from the Ni-Zr and Ni-Nb coordination, because the feature of the Ni coordination can be evaluated from the first nearest neighbour peaks at both the Nb and Zr K-edges, as discussed below. Secondly, the contribution of Ni-Ni to the peak cannot be ignored when taking the realistic structures of Ni-Zr and Ni-Nb bimetallic crystal alloys into consideration [48–53]. Therefore, the first nearest neighbour peaks of the FT spectra on the Ni K-edge probably consist of at least three components (Ni-Zr, Ni-Nb, and Ni-Ni). The first nearest neighbour peak at  $r \sim 2 \text{ \AA}$  of the FT spectra for the Nb K-edge is symmetrical in the shape, indicating that it consists of a single component (Fig. 5[b]). Judging from the reported atomic structures of NiNb crystal alloys [48, 49], it is reasonable to assign this peak to the Nb-Ni coordination. As can be seen in Fig. 5, there is a close resemblance between the FT spectra of Zr30-H0 and Zr30-H9 for each absorption edge. However, the FT spectra of Zr40-H0 are clearly different from those of Zr40-H11. The height of first nearest neighbour peak of the Zr40 alloy decreases significantly for all the three K-edges after hydrogen charging. There is also a significant difference between Zr40-H0 and Zr40-H9 in the shape of the FTs from the Nb and Zr K-edges around  $r = 2.6 - 3.5 \text{ \AA}$ . These results clearly indicate that essentially hydrogen doping does not alter the framework of the Zr30 alloy, but reasonably modifies that of the Zr40 alloy.

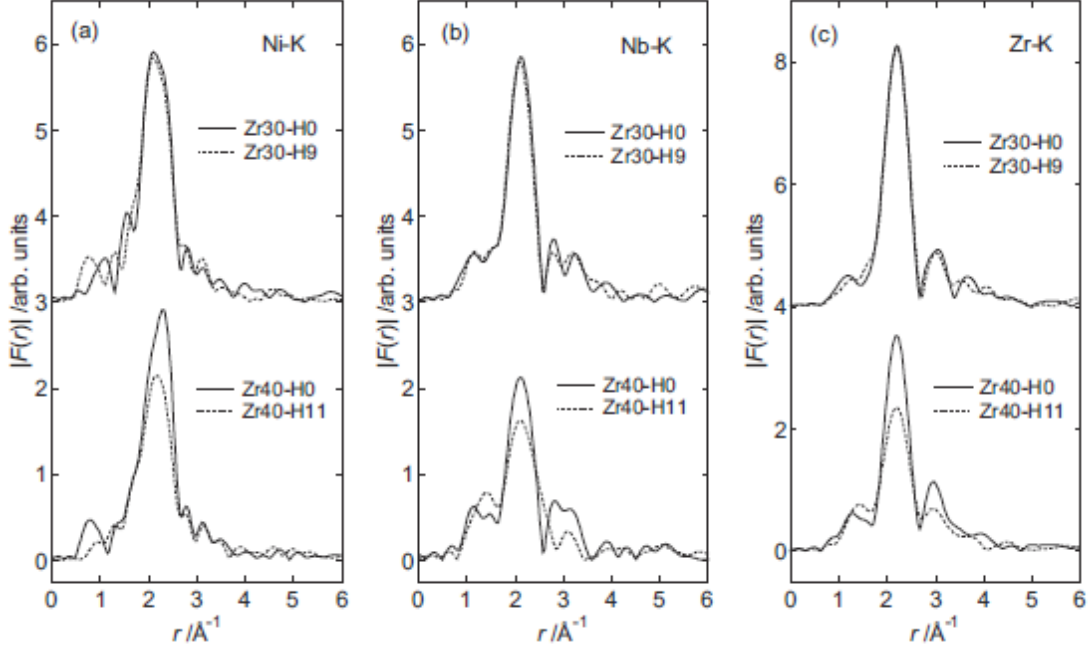


Fig. 5 The absolute values of Fourier transforms (FTs) the  $k^3$ -weighted XAFS oscillations ( $|F(r)|$ ) of Zr30-H0 (upper solid lines), Zr30-H11 (upper dotted lines), Zr40-H0 (lower solid lines), and Zr40-H11 (lower dotted lines) at the (a) Ni, (b) Nb, and (c) Zr K-edges. The FT ranges analysed are  $2.7 - 13.3 \text{ \AA}^{-1}$ ,  $3.0 - 12.0 \text{ \AA}^{-1}$ , and  $2.9 - 13.5 \text{ \AA}^{-1}$ , for Ni, Nb, and Zr K-edges, respectively.

In order to obtain the more quantitative structural parameters ( $N$ ,  $r$ ,  $\sigma^2$ ) around the core-excited atoms, fine analysis using curve-fitting techniques was carried out. The curve-fitting results for the Nb K-edge are summarised in Table 4. Only the closest neighbour peaks are treated in the ranges of  $R = 1.7 - 2.8 \text{ \AA}$  for the Zr40-H11 alloy and  $R = 1.7 - 2.5 \text{ \AA}$  for the other amorphous alloys in the curve fitting analysis. Here, we assume that each peak consists of one structural component (one-shell model), *i.e.* Nb-Ni alone, in the analysis [54]. The inter-atomic distances obtained are close to the Nb-Ni inter-atomic distance for the reported atomic structures of NiNb crystal alloys [48, 49]. For the Zr30 alloy, there are no differences in the inter-atomic distance ( $r$ ), the coordination number ( $N$ ), and the MSRD ( $\sigma^2$ ) between alloys with and without hydrogen within the analytical limits. However, the inter-atomic distance in the Zr40 alloys becomes longer, and the coordination number and MSRD become larger after hydrogenation. The peak corresponding to the closest neighbour has an asymmetrical form after the hydrogenation (see Fig. 5 (a)). This suggests that the two structural factors are contained in the closest neighbour peak of the Zr40-H11 alloy. Therefore, the “one-shell model” seems to be not appropriate for the Zr40-H11 alloy peak. The results of the curve-fitting analysis for the Zr K-edge are summarised in Table 5. The first and second nearest neighbour peaks are treated in the fitting analysis ( $R = 1.75 - 3.3 \text{ \AA}$ ). In the analysis, we assumed that these peaks consist of two components: *i.e.*, a “two-shell model”. The closest neighbour peak is more likely to only consist of Zr-Ni coordination. The second nearest neighbour peak probably consists of two major components: *i.e.*, Zr-Zr and Zr-Nb. However, we collected the two components in one shell. The functions  $F_i(k)$ ,  $\phi_i(k)$ , and  $\lambda_i(k)$  used in this shell are calculated by the Zr-Zr single scattering path. This treatment is valid because Nb and Zr adjoin in the atomic

number, resulting in a very small difference in the functions  $F_i(k)$ ,  $\phi_i(k)$ , and  $\lambda_i(k)$  between the Zr-Nb and Zr-Zr scattering paths.

Table 4 Results of the curve-fitting analysis for the Nb K-edge. The interatomic distances ( $r$ ), the coordination numbers ( $N$ ),  $\Delta E_0 = E - E_0$ , and the MSRDs ( $\sigma^2$ ) for all four amorphous alloys obtained by the analysis are shown. The values of  $R$ -factor are also given at the bottom of the table.

bond		Zr30-H0	Zr30-H9	Zr40-H0	Zr40-H11
Nb-Ni	$r/\text{\AA}$	2.55	2.54	2.54	2.59
	$N$	1.5	1.5	0.90	1.6
	$\Delta E_0/\text{eV}$	-5.3	-7.0	-6.3	-3.7
	$\sigma^2/\text{\AA}^2$	0.0086	0.0088	0.0069	0.013
$R$ -factor		0.0022	0.0031	0.0093	0.051

As can be seen in Table 5, the Zr-Ni bond lengths for the Zr30 and Zr40 alloys are almost identical (2.63 - 2.64 Å) independent of their hydrogen contents. The coordination numbers of the Zr30 alloys are significantly larger than those of the Zr40 alloys, thereby reflecting the difference in Zr-concentration between them. The Zr-Zr/Zr-Nb distances between the Zr30-H0 and the Zr30-H9 alloys are same within experimental accuracy. However, the Zr-Zr/Zr-Nb distance of the Zr40-H11 alloy is reasonably longer than that of the Zr40-H0 alloy by 0.08 Å. The hydrogen-induced expansion of the Zr-Zr distance have been also reported by Sakurai *et al.* [47] on  $(\text{Ni}_{0.6}\text{Nb}_{0.4})_{100-x}\text{Zr}_x$  ( $x = 30, 50$ ) amorphous alloys by the Zr K-edge XAFS and X-ray diffraction [55]. They have also been reported by Liu *et al.* [56] on  $\text{NiZr}_2$  by the Zr K-edge XAFS. Furthermore, the Nb-Ni distance of the Zr40-H11 alloy also expands when compared with the Zr40-H0 one, although there is no report on this.

Table 5 Results of the curve-fitting analysis for the Zr K-edge. For details, see the caption for Table 5.

bond		Zr30-H0	Zr30-H9	Zr40-H0	Zr40-H11
Zr-Ni	$r/\text{\AA}$	2.63	2.64	2.63	2.64
	$N$	3.3	3.6	2.6	2.2
	$\Delta E_0/\text{eV}$	-7.0	-6.3	-7.5	-10.3
	$\sigma^2/\text{\AA}^2$	0.011	0.012	0.011	0.013
Zr-Zr or Zr-Nb	$r/\text{\AA}$	3.24	3.25	3.25	3.33
	$N$	5.4	4.8	5.1	5.0 <sup>a)</sup>
	$\Delta E_0/\text{eV}$	2.3	2.9	1.8	-0.1
	$\sigma^2/\text{\AA}^2$	0.025	0.025	0.022	0.024

The difference in the structural response between Zr30 and Zr40 alloys probably comes from the difference in the site where the hydrogen atoms are located. In the Zr30 alloy, hydrogen atoms

plunge somewhere outside the clusters, since no significant changes in bond length was observed. The elongation of Zr-Zr/Zr-Nb and Nb-Ni distances in the Zr40-H11 alloy is associated with an occupation of hydrogen in tetrahedral sites surrounded by Zr and Nb, or Zr, Nb, and Ni atoms. For the Ni K-edge, the closest neighbour peak is probably derived from at least three contributions (Ni-Ni, Ni-Nb, and Ni-Zr), as discussed above. Consequently, the number of the fitting parameters becomes so large that we could not obtain reliable fitting results, even if the inter-atomic distances and MSRDs of Ni-Nb and Ni-Zr are constrained to those obtained in the fitting analysis of the Nb and Zr K-edges. To enhance the performance of the curve-fitting analysis on the data of the Ni K-edges, we must increase restriction condition for the fitting parameters. This will allow us to construct concrete atomic cluster models.

It is known that icosahedron-like polyhedra play an important role in stabilising the structure of metal-metal type amorphous alloys [57]. With this fact in mind, we will discuss possible structural models for the Ni-Nb-Zr amorphous alloy studied here. Firstly, we will examine the model reported by Fukunaga *et al* [57]. Their results of the analysis of Voronoi polyhedra in the reverse Monte-Carlo (RMC) simulation based on the data of neutron and X-ray diffraction indicate that all the Zr atoms in the  $\text{Ni}_{25}\text{Zr}_{60}\text{Al}_{15}$  amorphous alloy are mostly surrounded by icosahedra or icosahedron-like polyhedra. This means the average coordination number for Zr atom is *ca.* 12. However, the coordination numbers estimated from our XAFS results are 7.2–8.7. Therefore, Fukunaga's model is inconsistent with our results of the XAFS analysis. We will also discuss a model in which the icosahedral or icosahedron-like clusters are randomly packed. In this model, the contribution from the atoms in neighbouring clusters to the FT spectra of XAFS will be negligibly small, because it is evident that the positional correlation between the atoms in one cluster and in another will be weak in an amorphous state. The coordination numbers observed using XAFS account for the configuration of the atoms within a cluster. In the analysis of the Zr K-edge XAFS spectra of the Ni-Nb-Zr amorphous alloys, Sakurai *et al.* [47] presumed that the second closest neighbour peak in FT spectra is mostly comes from the Zr-Zr bonds, and the contribution from Zr-Nb is negligible. This means that the Zr and Nb atoms are not directly bonded. The icosahedral cluster model satisfying this condition (hereafter referred to as model-(a)) is depicted in Fig. 6(a). The average coordination numbers calculated for the model-(a) are listed in Table 6, together with the coordination numbers estimated by the XAFS analysis for the Zr30-H0 and Zr40-H0 alloys. As given in Table 6, the average coordination number of 6 for Nb-Ni estimated from the model-(a) is apparently large in comparison with the values obtained by XAFS analysis. Furthermore, the content ratio of Nb to the other atoms (Zr and Ni) in the cluster is too small when taking the actual chemical compositions of the Zr30 and Zr40 alloys into consideration. Therefore, it is more likely that the second neighbour peak of the Zr K-edge also includes the inevitable component of Zr-Nb as well as that of Zr-Zr. As the previous models described above do not explain the analysis results of the XAFS spectra, we propose two probable cluster models for the Zr-Nb-Ni ternary amorphous alloys as depicted in Figs. 6(b) and (c) (hereafter referred to as models-(b) and (c), respectively). In fact, the average coordination numbers calculated for both the cluster models (Table 6) fairly agree with the coordination

numbers estimated by XAFS. It should be noted that the shape of the icosahedron should be distorted, since the bond-lengths of Zr-Ni, Nb-Ni, Zr-Zr, and Zr-Nb are different among them, as shown in Fig. 6. In both models, the maximum numbers of hydrogen atoms that can be stored in the clusters are different. From the XAFS analysis, it is difficult to determine which model is more preferable, since the difference between the coordination numbers calculated for models-(b) and (c) is so small when obtained by XAFS analysis. The distorted icosahedral cluster(s) of models (b) and (c), or a combination of them will be the main constituent of the amorphous alloys. The addition of hydrogen atoms has no significant effect on the atomic configuration in Zr30 alloy, but dies on the Zr40 one. This suggests that hydrogen atoms occupy only the sites outside the Ni-Nb-Zr clusters in Zr30 alloys, but both inside and outside the clusters in Zr40 alloys. This difference in the location of hydrogen atoms possibly comes from a certain structural difference between Zr30 and Zr40 alloys. Although we have not had a clear picture yet, there may be a structural difference in the cluster itself and/or in the interstitial space outside the cluster defined by the manner in which clusters are arranged in the alloys.

Table 6 Average coordination numbers calculated for three cluster models. The structures of model clusters are illustrated in Fig. 5. The coordination numbers estimated by XAFS analysis are also shown.

Edge	Bond	Model			XAFS	
		(a)	(b)	(c)	Zr30-H0	Zr40-H0
Nb K	Nb-Ni	6	1.67	2.33	1.5	0.90
	Nb-Nb					
	or	0	4.33	3.67	--	--
Zr K	Nb-Zr					
	Zr-Ni	2.6	2.2	2.6	3.3	2.6
	Zr-Zr					
	or	3.4	5	4.6	5.4	5.1
	Zr-Nb					

From the structural change of the hydrogenated alloys observed by XAFS analysis, we can decide the occupation sites of hydrogen, as indicated by small gray solid circles in Fig. 6. In the upper part of the clusters, hydrogen atoms are settled into the tetrahedron sites that are surrounded by three Zr atoms and one Nb atom, since the Zr-Zr and Zr-Nb bonds expand after hydrogenation. The Nb-Ni bond also lengthens by hydrogenation. Thus, the hydrogen atoms are plunged into a near Nb atom in tetrahedral sites in the lower part of the clusters. More hydrogen atoms occupy the upper side. Considering the stoichiometry, these sites will be partially occupied by the hydrogen atoms in the Zr40-H11 alloy. The atomic radii of Ni, Nb, and Zr in the crystalline form are 1.24, 1.45, and 1.60 Å, respectively [58]. Therefore, the atomic distances of Nb-Ni and Zr-Ni in the Ni-Nb-Zr amorphous alloys obtained in the present study (2.54 - 2.55 and 2.63 Å, respectively) are considerably shorter than those calculated from the crystalline atomic radii (2.69 and 2.84 Å, respectively). This is an important point for application of amorphous alloys, such as

super-conductivity and ballistic transport. Furthermore, dropping a hydrogen atom into the designated tetrahedral site induces shrinkage of the atomic distances in the neighbour sites, as a high pressure effect. This also provides another important effect for atomic structural elucidation of the various electronic transport behaviours [36] in the Ni-Nb-Zr glassy alloys of interest.

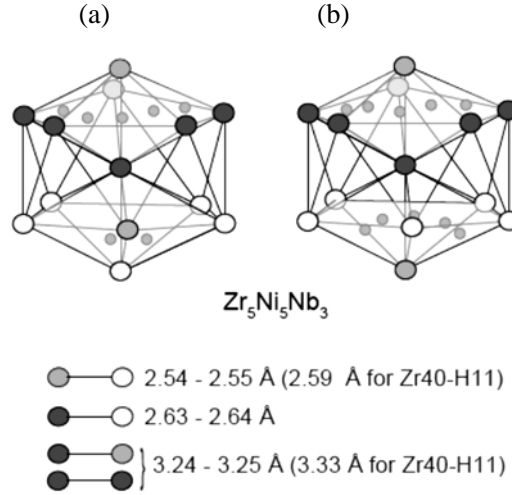


Fig. 6 Cluster models with an icosahedral structure and the chemical compositions of  $\text{Ni}_5\text{Nb}_3\text{Zr}_5$  (a, b). The sites that can be occupied by hydrogen atoms are also indicated by small gray circles. The bond-lengths obtained by the XAFS analysis are indicated in the bottom part.

### 3.2 Structures of the icosahedral clusters by first-principles molecular dynamics calculation and XAFS measurements [59]

In the previous section, we considered that hydrogen atoms in the Zr30at.% alloy plunge into a space somewhere outside the clusters, based on the fact that there is no change in the bond length, while the elongation of the Zr–Zr/Zr–Nb and Nb–Ni distances in the  $(\text{Ni}_{36}\text{Nb}_{24}\text{Zr}_{40})_{0.89}\text{H}_{0.11}$  (Zr40-H11) alloy are associated with the occupation of the tetrahedral sites surrounded by Zr and Nb or Zr, Nb, and Ni atoms by hydrogen in the clusters [46, 41]. In fact, the Zr40at. % alloy showed room temperature Coulomb oscillation when it was hydrogenated, while the Zr30at. % alloy did not [37]. Therefore, the origin of the difference in the electronic properties of these alloys lies in the structural difference between them. Especially, the spectra of the pre-edge region reflect the electronic structure of the relevant ion and its surroundings, as is well known. We found that the hydrogen atoms occupy highly symmetric sites in Zr40-H11 to prevent the  $d$ - $p$  mixing, and that hydrogen atoms principally surround the Zr and Nb atoms [60].

In the section, we will discuss in detail a possible cluster model for the amorphous alloys. First, we will examine the XAFS data again and we will focus on the X-ray absorption Near Edge Structure (XANES) spectra, in order to extract further structural information, especially related to the possible position of the hydrogen atoms inside the cluster. Also, the results of the cluster simulation of the Zr40at. % alloy using first-principles calculations are presented. This gives a more probable hydrogen position than the model proposed based on the analysis of the extended X-ray absorption fine structure (EXAFS) and XANES spectra. The stable hydrogen sites are discussed based on the results of the XAFS and theoretical simulation.

The optimised atomic configurations of the icosahedral clusters that consisted of Ni, Nb, Zr and H atoms were determined by VASP: a plane-wave-based first-principles molecular dynamics calculation package [61]. We employed the ultrasoft pseudopotential for the core orbitals [62] (1s-3p for Ni and 1s-4p for Zr and Nb) under the generalised gradient approximation (PW91 [57]). The cutoff energy for the plane wave basis was 241.622 eV (NORMAL precision in VASP). The isolated cluster system was realised in a supercell with the  $\Gamma$ -point approximation. A length of more than 10 Å was adopted for the cell dimension. A quasi-Newtonian algorithm was used to relax the ions until the change in the total energy reached below  $10^{-3}$  eV between the two ionic steps. The results of the simulation were compared with those of the XAFS analysis to construct the optimum cluster model.

The electronic states around the outmost shell of the absorbing atom should be reflected in the pre-edge energy region, where transitions from a 1s orbital to an  $nd$ , an  $(n+1)d$  and an  $(n+1)p$  state can be observed in the transition metals. The former two transitions are essentially forbidden, while the last one is allowed for the electric dipole moment. Therefore, the absorption intensities of the former two transitions are weak, but very sensitive to the alignment symmetry of the surroundings. A few pre-edge peaks were often observed in the XAFS spectra of transition metal compounds. Weak but explicit pre-peaks were sometimes found, and were assigned to the transition to the  $nd$  states. Figure 7 shows the absorption spectra around the K-edge of Ni, Nb, and Zr, respectively, for the Ni-Nb-Zr-H amorphous alloys. A shoulder accompanies the rising of each absorption edge, except in the case of the Zr40-H11 alloy. The energy position of the shoulder is in the range of 1~5 eV below the edge is determined as having half the intensity of the edge jump. Therefore, it is reasonable to assign the shoulder peaks to the parity forbidden transition to the 3d orbital (Ni) and the 4d orbital (Nb and Zr). The transition moment to the orbitals generally does not reach zero, due to the crystal (ligand) field with odd parity or the lattice vibration (phonon) of odd parity modes in solids. As can be seen in Fig. 7, the intensity of the shoulder for the Zr30at. % alloy remains unchanged in hydrogenation at all three absorption edges. However, the Zr40at. % alloy is substantially weakened by hydrogenation at the Nb and Zr K-edges, although less affected at the Ni K-edge. Turning our attention to the post-edge energy region in the XANES spectrum, a difference between Zr30% and Zr40% was similar to that in the pre-edge region on the hydrogenation of the alloys. The difference in the post-edge region for the XANES spectrum would include structural information on the cluster backbone, which is complementary to the information given by the EXAFS spectra. Moreover, the scattering caused by light elements such as H, He, and Li diminished at a low wavenumber, because the back-scattering amplitudes rapidly decreased with the wavenumber of the photoelectrons. Since the kinetic energy of the photoelectrons in the XANES region was much lower than that in the EXAFS region, the spectra were directly and considerably affected even by these light elements. For these reasons, the XANES part of the XAFS spectra was more sensitive to the coordination of the H atoms than the EXAFS part. Therefore, we were also able to inspect the effects of hydrogenation on the structure from the post-edge XANES spectra.



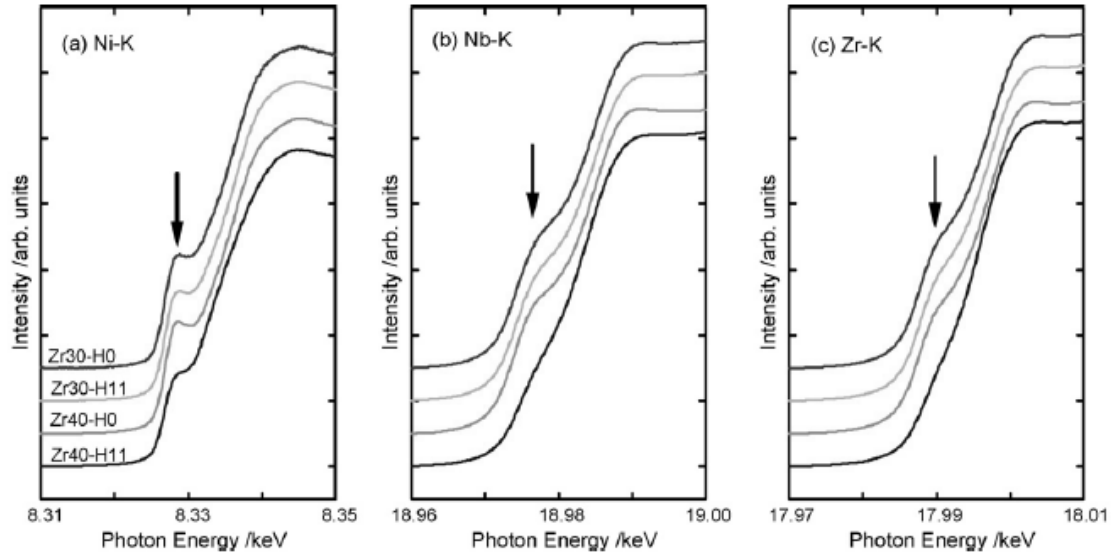


Fig. 7 Close-ups of the pre-edge peaks in the XANES spectra of the amorphous alloys at the (a) Ni, (b) Nb, and (c) Zr K-edges.

As shown in Fig. 8, the post-edge spectrum of the Zr40at. % alloy for the Ni K-edge was less affected by hydrogenation. However, those for the Nb and Zr K-edges were rather strongly modified by the hydrogenation. In the case of the Zr30 at.% alloy, almost no change was observed upon hydrogen doping. Here, it should be noted that the modification of the spectrum by the charged hydrogen showed a similar tendency for both Nb and Zr K-post-edges. This finding implies that the multi-scattering paths of the hydrogen atoms surrounding these metal atoms were analogical: that is, the hydrogen atoms coordinated around these metal atoms in a similar electronic configuration in both cases. The results shown in Fig. 8 are consistent with the structural configurations yielded by the XANES analysis, shown in Fig. 7. The results of the XANES analysis described above strongly suggest the following several points: i) in Zr30at. % amorphous alloys, the hydrogen atoms do not localise inside, but outside the clusters; ii) the hydrogen atoms rarely localise the position around Ni atoms; iii) the hydrogen atoms occupy suitable sites in the clusters in the Zr40at. % alloy, and localise around the Nb and Zr atoms but not around the Ni atoms; iv) the sites occupied by the hydrogen atoms are positions which prevent  $p - d$  hybridisation.

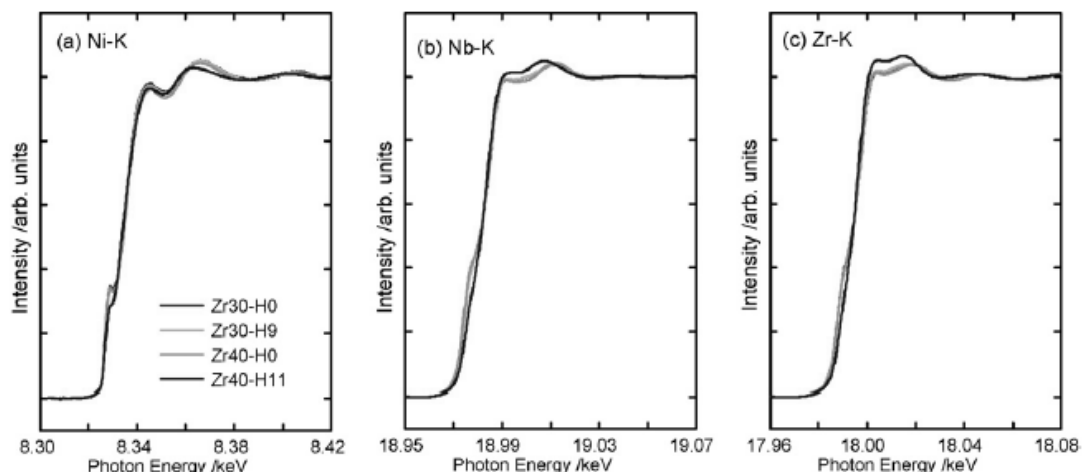


Fig. 8 XANES spectra of the amorphous alloys at (a) Ni, (b)Nb and (c)Zr K-edges, including pre- and post-edge regions.

To clarify the mechanism of the room-temperature Coulomb oscillation observed in  $(\text{Ni}_{0.36}\text{Nb}_{0.24}\text{Zr}_{0.40})_{90}\text{H}_{10}$  amorphous alloy, we will focus on the Zr40 % sample with hydrogen in this section. Applying the coordination numbers obtained from the XAFS analysis results to the cluster model simulation by first-principles calculations, we reconstructed the atomic cluster model. It is well known that the atomic clusters of metal/metal-typed amorphous alloys are characterised by a Zr-centred icosahedral structure [36]. So, we will focus on isolated icosahedral Zr-centred  $\text{Ni}_5\text{Nb}_3\text{Zr}_5$  clusters, whose composition is close to that of the  $\text{Ni}_{36}\text{Nb}_{24}\text{Zr}_{40}$  alloy [40]; this is assuming that the energy of the hydrogen on the surface of the cluster is not significantly changed by the presence of neighbouring clusters [41]. Real clusters are combined with small amounts of other Voronoi-like polyhedra: *i.e.*, they are not isolated [36]. The four possible structural models are presented in Table 7, along with the total binding energies, which are given for each structural model in the order of stability. The four kinds of models are shown in Fig. 9 through a side and top view. The relationships between the coordination numbers of the Zr-Zr (or Zr-Nb) and Nb-Ni bondings, on the one hand, and the coordination numbers of the Zr-Ni bonding, on the other, are shown in Fig. 10. When applying the calculated coordination numbers for the four kinds of clusters to the experimental ones, the coordination numbers of Ih553z and Ih553i agree well with those determined by the XAFS analysis. Therefore, the Ih553z and Ih553i cluster are candidates for the main intrinsic cluster. From the energetic point of view, the Ih553i cluster is more feasible, as seen in the total energies listed in Table 8. However, as seen in Fig. 9, the shape of Ih553i and Ih553z is distorted relative to the ideal icosahedron shape. In comparison with two models, the Ih553z cluster is slightly more stable than the Ih553i one. Therefore, we currently believe that the Ih533z cluster is the most probable cluster.

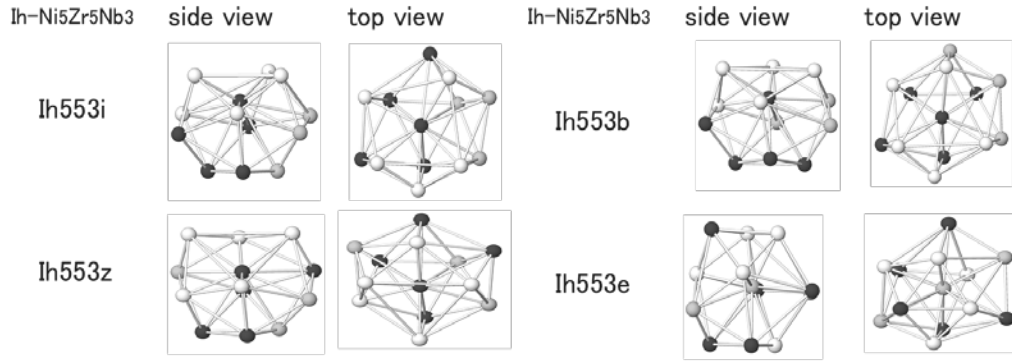


Fig. 9 Side and top views of the four stable kinds of simulated  $\text{Ni}_5\text{Zr}_5\text{Nb}_3$  clusters. The solid circles represent Zr atoms (black), Nb atoms (gray), and Ni atoms (white).

Table 7 Comparison between the calculated and the experimental coordination numbers for the Zr-Ni, Zr-Zr or Zr-Nb and Nb-Ni bindings in four kinds of simulated clusters.

Cluster type		Centered element	Coordination numbers		
Cluster type	Total binding energy (eV)		Zr-Ni	Zr-Zr or Zr-Nb	Nb-Ni
1. Ih553i	-79.8289	Zr	2.40	4.80	1.00
2. Ih553z	-79.157	Zr	2.60	4.60	1.67
3. Ih553b	-78.8349	Zr	1.40	4.60	2.00
4. Ih553e	-77.2815	Zr	2.00	5.20	3.33

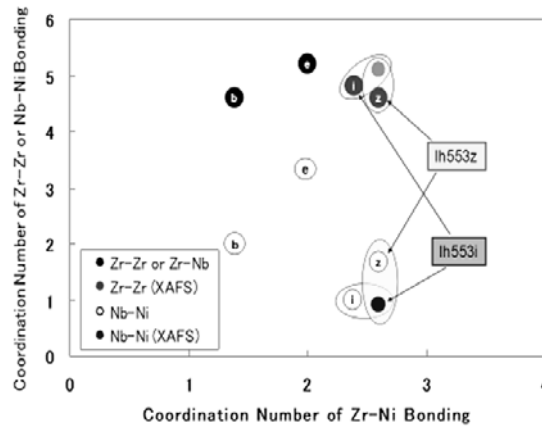


Fig. 10 Comparison between the calculated and the experimental coordination numbers for the Zr-Zr or Zr-Nb and Nb-Ni bindings in four stable types of simulated clusters.

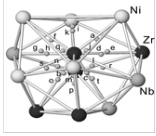
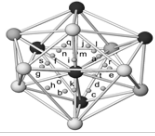
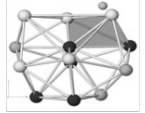
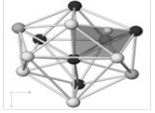
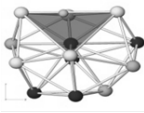
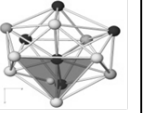
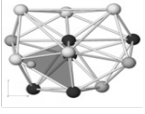
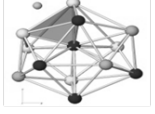
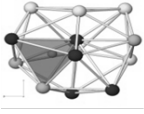
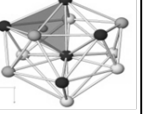

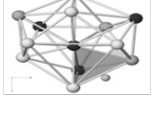
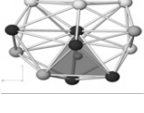
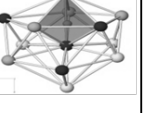








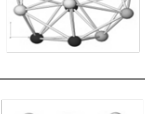
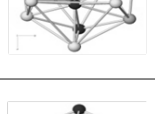
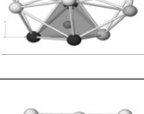
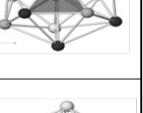
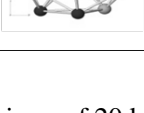


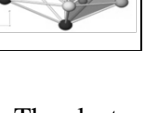
facet H-distance (Å)	side view	top view	facet H-distance (Å)	side view	top view
Indices of hydrogen atoms					
(a) NiNiZr			(k) NiNiNi		
+ 0.98			+ 0.85		
(b) NiNiZr			(l) ZrZrNb		
+ 0.96			- 0.66		
(c) NiNiNb* (NiZrNb)			(m) ZrZrNb		
+ 0.64			- 0.69		
(d) NiNiNb			(n) ZrZrNb		
+ 0.54			- 0.71		
(e) NiNiNb* (NiZrNb)			(o) NiZrZr		
+ 0.83			- 0.32		
(f) NiNiNb			(p) ZrZrNb		
+ 1.04			- 0.67		
(g) NiNiNb			(q) NiZrNb		
+ 0.87			- 0.56		

Fig. 11 The side and top views of 20 kinds of simulated  $\text{Ni}_5\text{Zr}_5\text{Nb}_3$  clusters with H atom. The clusters are in the order of stability. The distance from the facet surface of the cage is also shown. The plus sign of the distance denotes running away from the centre of the grey tetrahedral cage, while larger negative values mean stable localisation of hydrogen in the one.

Next, we simulated the possible localisation site of hydrogen in the hypothetical Ih553z icosahedron. A hydrogen atom was placed at the centre of one of the 20 tetrahedron cages as its initial position (distance from the central Zr atom = 1.32 Å). Then, the position of the H atom was optimised relative to the fixed cages. When one hydrogen atom plunged into a tetrahedral site in the Ih553z icosahedron, the total energy of the Zr-Ni-Nb-H network changed depending on the combination of the three constituent elements of the for tetrahedron. The optimised positions of

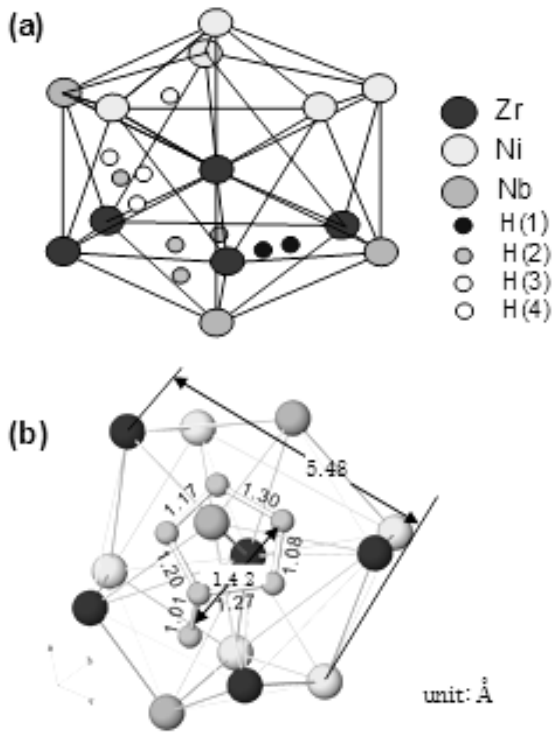


Fig. 12(a) Hydrogen-occupied icosahedron cluster (Ih553z) model, and (b) the distances among two stable and four metastable H sites.

the H atom in the 20 possible kinds of  $\text{Ni}_5\text{Zr}_5\text{Nb}_3$  (Ih553z) configurations are presented in Fig. 11, along with the distance from the facet surface of the cage. It should again be noted that the initial position of the H atom was set at the center of the purple tetrahedral cage. A plus sign on the distance denotes movement away from the tetrahedral cage, while larger negative values mean the stable localisation of the hydrogen atom in the cage. Actually, the hydrogen atom in Fig. 15(c) and (e) moves away from the tetrahedrons composed of two or three Ni elements ((a)-(i) and (k) in Fig. 11), and settles inside the tetrahedron with zero or one Ni atom ((j)). As a result, the order of stability of the hydrogen site in the tetrahedrons is as follows: two Zr-Zr-Nb-Nb ((r) and (t)); four Zr-Zr-Zr-Nb ((l)-(n) and (p)); two Zr-Zr-Nb-Ni ((q) and (s)); and two Zr-Zr-Zr-Ni ((j) and (o)) tetrahedrons. Since

Ni has an anti-affinity for hydrogen, the sites of the last two Zr-Zr-Ni-Ni tetrahedra are metastable, while the sites of the two Zr-Ni-Ni-Ni and Zr-Nb-Ni-Ni tetrahedral afford negligibly small stability. These results for the optimum hydrogen site are summarised in Fig. 12, alongside the ten hydrogen atoms. For clarity, the model cluster is illustrated in the regular icosahedron shape in the figure, although it is distorted in reality. The distances of inter hydrogen atoms among the two stable and four metastable H sites are presented in Fig. 12(b).

From the calculated adiabatic potential energy of the hydrogen atom for the distorted icosahedral  $\text{Ni}_5\text{Zr}_5\text{Nb}_3$  cluster with hydrogen, it was concluded that the potential energy of hydrogen was adsorbed by the outer surface of the cluster, which was lower than that of the bonding state between Zr (or Nb) and the H atoms settled in the cluster [41, 63]. In other words, the outer adsorbed hydrogen from the cluster is in a stable state, while the inner bonding hydrogen in the tetrahedron is in a metastable state. Indeed, the hydrogen atom localised to a site between the clusters in alloys with a hydrogen content of approximately 5%, and inside the clusters in alloys with a hydrogen content of between 7% and 12.5 % [41]. The above calculation results are in good agreement with the XANES results on the affinity elements for hydrogen.

It is known that icosahedral clusters with a size of  $\sim 1$  nm exist in metal/metal-type Zr-based amorphous alloys with a Zr-centred cluster [36]. Since our model, Ih553z, is a Zr-centred icosahedral  $\text{Ni}_5\text{Zr}_5\text{Nb}_3$  cluster with a maximum size of 0.55 nm, the atomic configuration agrees with the results of the XAFS analysis, as shown in Fig. 9. The amorphous alloy used in the present study consists of antinomic elements (*i.e.*, Zr and Nb show affinity and Ni anti-affinity for hydrogen). Indeed, the enthalpies of the dissolved hydrogen atoms for Zr, Nb, and Ni are -63, -34, and +16 kJ/mol H, respectively [64]. Therefore, we must take the antinomy into consideration when we examine the structure of icosahedral clusters with hydrogen as well as conventional hydrogenated crystals. As can be seen from the sign of the distance from the facet surface of the cage in Fig. 11, the most stable localisation site for hydrogen is the tetrahedral site formed by two Zr and two Nb atoms, while the tetrahedron consisting of three Zr atoms and one Nb atom is of secondary stability. The hydrogen is less stable if it is at a tetrahedral site that includes at least one Ni atom. Therefore, the distorted  $\text{Ni}_5\text{Zr}_5\text{Nb}_3$  cluster of interest is characterised by five Ni atoms, which form half a pentahedron and an opposite pentahedral Zr-Nb assembly, because the theoretical simulations indicate that the gathering of Ni atoms in the icosahedra lowers the total energy. The nanometre-sized strangely shaped icosahedral clusters and their atomic configurations seem to be the source of functional properties, such as the Coulomb oscillation [36-38, 65-68] in Chapter 4, ballistic transport behaviours [41, 69] in Chapter 5, and super-conductivity [36, 70] in Chapter 6.

### ***3.3 Structures and electronic properties of $\text{Ni}_5\text{Nb}_5\text{Zr}_5$ clusters in Ni-Nb-Zr amorphous alloys [71, with kind permission of The European Physical Journal (EPJ)]***

In this section, we will calculate the electronic states of the icosahedral  $\text{Ni}_5\text{Nb}_5\text{Zr}_5$  clusters and optimise the structures by using the first principles calculation. To check and compare the supercell calculation with isolated cluster calculation, we will employ the ADF package with the LCAO-GGA scheme [72]. The ADF package is also used for DOS calculation and population analysis. The initial structure of the  $\text{Ni}_5\text{Nb}_3\text{Zr}_5$  is taken as an icosahedron with the interatomic distance of 2.50 Å between the center and the surrounding atoms (2.63 Å between surrounding atoms). Then the structures are fully optimised by the quasi-Newton algorithm until the change in the total energy is smaller than  $10^{-4}$  eV between the two ionic steps.

Figure 13 shows the total energies of twenty-five optimised clusters as a function of Nb-Ni CN (number of Ni atoms surrounding a Nb atom): (a) for Ni-centred, (b) for Nb-centred, and (c) for Zr-centred clusters. The vertical lines indicate the CN, 0.9, obtained by XAFS method [40]. Comparing three types of the centre atom, the Ni-centred clusters are more stable in general. This is mainly due to a small atomic radius of Ni atoms, 1.25 Å (cf. 1.43 Å for Nb, 1.59 Å for Zr). Figure 13 also shows, especially for the Ni-centred cluster in Fig. 13 (a), that a smaller CN in the Nb-Ni makes the cluster more stable. This tendency agrees with the remarkably small number of the experimental result, 0.9. For Nb-centred clusters, the CNs of Nb-Ni are obviously larger than in the experimental one, and never come close to that value. The optimised structure of the most stable Ni-centred cluster, as shown by the inset in Fig. 13(a), keeps its icosahedral shape whereas